Grain size reduction by plug flow in the wet oceanic upper mantle explains the asthenosphere's low seismic Q zone

Florence D. C. Ramirez[1,2,*], Clinton P. Conrad[1] and Kate Selway[1,2,3]

[1] Centre for Earth Evolution and Dynamics, University of Oslo, Norway
[2] Department of Earth and Environmental Sciences, Macquarie University, Australia
[3] Future Industries Institute, University of South Australia

Supplementary Information

A. Predicted seismic structures for non-deforming oceanic upper mantle

For an oceanic upper mantle that is not deforming, we assume that the grain size is constant. We consider different grain sizes (1 mm – 10 cm) and calculate their respective seismic depth profiles (blue lines, Figure S1).

We calculate the shear wave velocity V_s and seismic quality factor Q as a function of depth for different grain sizes. We estimate V_s as (Karato, 1993):

$$V_s = V_\infty(T, P) \left[1 - \frac{1}{2} \frac{\cot(\pi\alpha/2)}{Q(\omega, T, P, d)} \right] \tag{S1}$$

where V_∞ is the velocity at infinite frequency, α is a non-dimensional constant of 0.274, T is temperature, P is pressure, d is grain size, and ω is frequency for a period that scales with depth (period(s) = depth(km)/1.4). The parameter V_∞ is calculated using the
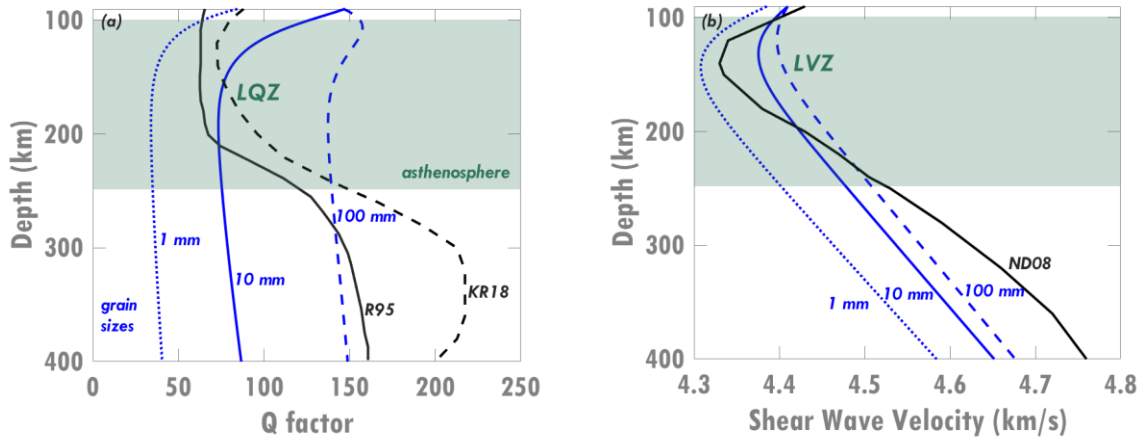

Figure S1. Seismic depth profiles for oceanic upper mantle that is not deforming. (a) The seismic Q depth profiles (blue lines) are calculated using Jackson and Faul's (2010) formulation for period increasing with depth (period = depth(km)/1.4), where Q is sensitive to a chosen grain size (values given), which is assumed constant in the absence of deformation. The global KR18 (dashed black line) and R95 (solid black line) models are from Karaoglu & Romanowicz (2018) and Romanowicz (1995), respectively, which both show a low seismic Q zone (LQZ) in the asthenosphere. (b) The associated forward shear wave velocities (blue lines) are estimated using Karato's (1993) formulation (Equation S1), again for constant chosen grain size. The global ND08 model (black line) is from Nettles & Dziewonski (2008), which shows a low-velocity zone (LVZ) within the asthenosphere.

* Corresponding author at: Centre for Earth Evolution and Dynamics (CEED), University of Oslo, Sem Sælands vei 2A, 0371 Oslo, Norway
Email address: f.d.c.ramirez@geo.uio.no

formulation of Stixrude and Lithgow-Bertelloni (2005), which is suitable for oceanic upper mantle with pyrolytic composition:

$$V_\infty(T, P) = 4.77 + 0.038P - 0.000378(T - 300) \qquad (S2)$$

The seismic Q factor is calculated using the grain-size dependent formulation of Jackson and Faul (2010) with the parameter values summarized in Table 2 of their paper, except that we chose an activation volume of $V_Q = 6 \times 10^{-6}$ m^3/mol as discussed in Section B. To implement the calculation correctly, we have replicated the results of Jackson and Faul (2010), particularly their Figures 3 and 4.

As expected, Q values (Figure S1a) within the upper mantle are larger for larger grain size, resulting in faster seismic velocities (Figure S1b) than for smaller grain size. Notably, a low-velocity zone (LVZ) can be produced (Figure S1b) but not the low seismic Q zone (LQZ, Figure S1a).

B. Effect of activation volume on seismic structures

Flow-induced grain sizes depend on the activation volume for grain growth V_g, which controls the enthalpy required to start grain growth. A larger V_g (12×10^{-6} m^3/mol) makes grain growth slower than a smaller V_g (4×10^{-6} m^3/mol), resulting in smaller grain sizes (light vs. dark lines, Figures S2a and S2c). Since our Q calculation is grain-size dependent, the choice of V_g affects the Q profile (Figures S2b and S2d), with a smaller V_g resulting in larger Q due to larger grain sizes (dark lines, Figures S2).

The effect of pressure on seismic Q is expressed by V_Q, which is the activation volume for (anelastic and viscous) relaxation times. Theoretically, this activation volume decreases with increasing pressure (e.g., Sammis et al. 1981; Hirth and Kohlstedt 2003). However, activation volume is not well-constrained by laboratory experiments, so we assume a constant activation volume with depth. Different choices are also possible that can forward model seismic Q trends that are comparable with global observations. Here we consider two activation volumes (V_Q of 6×10^{-6} m^3/mol and 10×10^{-6} m^3/mol) that are within the range of the available estimates (e.g., Sammis et al. 1981; Hirth and Kohlstedt 2003; Faul and Jackson 2005), and investigate their impact on seismic depth profiles for dry (Couette flow or *CF*-dominated, Figure S2b) and wet (plug flow or *PFn3*-dominated, Figure S2d) upper mantle. Smaller V_Q (solid dark lines) results in smaller Q than larger V_Q (dashed dark lines). A LQZ in the asthenosphere, as observed in global models (black lines, Figures S2b and S2d), is better produced by a larger $V_Q = 10 \times 10^{-6}$ m^3/mol for dry and *CF*-dominated upper mantle (dashed dark line, Figure S2b) and a smaller $V_Q = 6 \times 10^{-6}$ m^3/mol for wet and *PFn3*-dominated upper mantle (solid colored lines, Figure S2d). However, the predicted minimum Q in the asthenosphere is closer to the seismic observations for smaller V_Q (for both wet and dry conditions, Figures S2b and S2d), and thus we use $V_Q = 6 \times 10^{-6}$ m^3/mol in the following calculations ("preferred" model in Figure S2). For the activation volume for

grain growth, we use $V_g = 4 \times 10^{-6}\,\text{m}^3/\text{mol}$ as a "preferred" value (Table S1). However, a larger value of V_g results in smaller grains and smaller Q, and may be important for explaining seismic observations in wet conditions (Figure S2c).
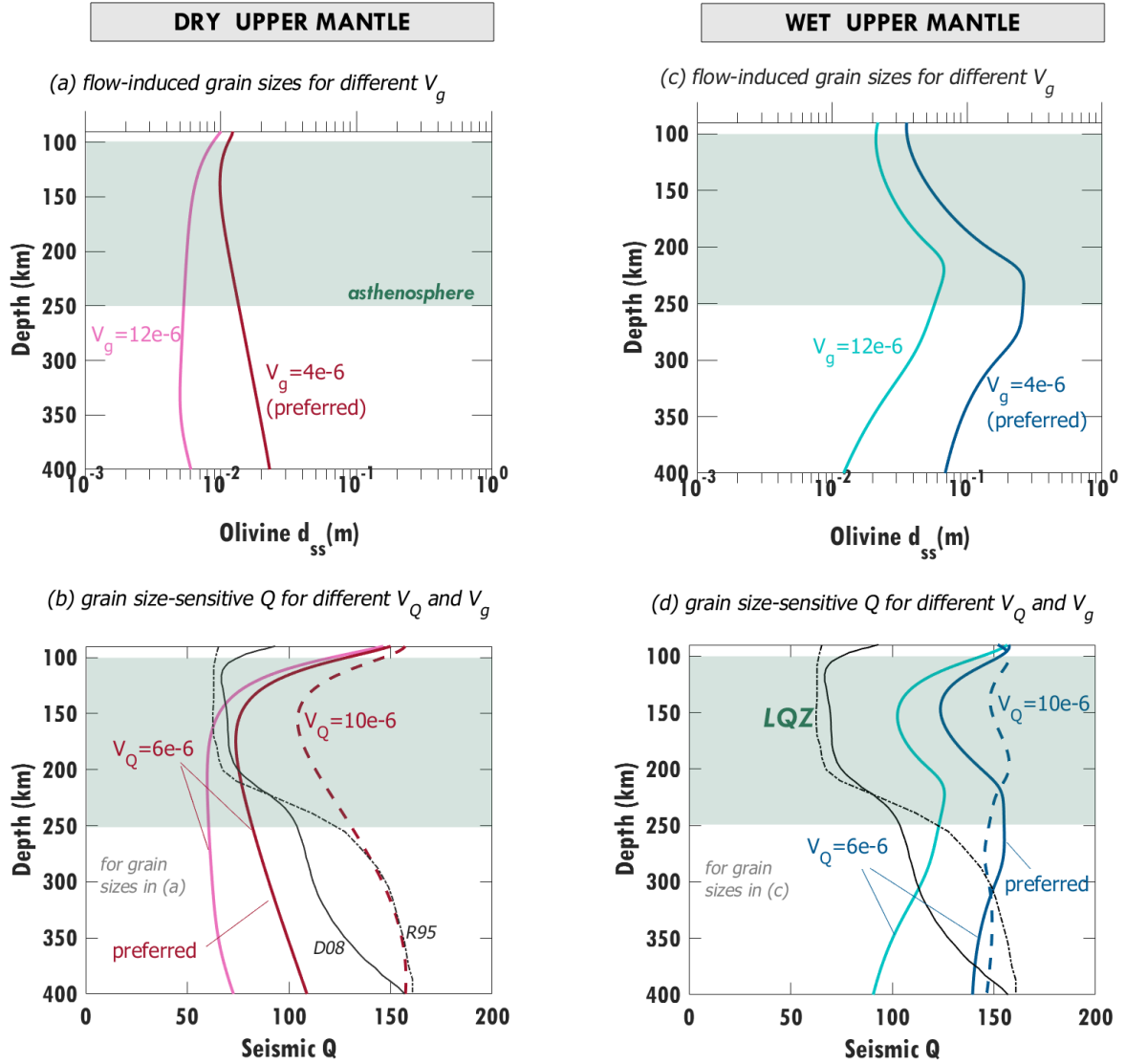

Figure S2. Effect of activation volumes V_g and V_Q on predictions of Q for dry and wet upper mantle. Q is calculated using Jackson and Faul's (2010) formulation with the parameter values summarized in Table 2 of their paper and the steady-state grain sizes shown in panels (a) and (c) for dry and wet upper mantle, respectively. These grain-size profiles are computed for mantle below 60 Myr old lithosphere and are produced by *CF* (Couette flow) in dry upper mantle (a) and *PFn3* (plug flow) in wet upper mantle (c), both driven by a 2-cm/yr moving plate and a -1 kPa/km pressure gradient (case i, Figure 4). We have utilized two activation volumes for calculating Q (b and d), $V_Q = 6 \times 10^{-6}\,\text{m}^3/\text{mol}$ (solid lines) and $10 \times 10^{-6}\,\text{m}^3/\text{mol}$ (dashed lines), and two activation volumes for grain growth $V_g = 12 \times 10^{-6}\,\text{m}^3/\text{mol}$ (light colored lines) and $4 \times 10^{-6}\,\text{m}^3/\text{mol}$ (dark colored lines). Shown for comparison in (b) and (d) are observations of seismic Q from the R95 global Q model of Romanowicz (1995) and the D08 model of Dalton et al. (2008) for mid-age oceans, which both indicate a low Q zone (LQZ) in the asthenosphere. The 'preferred' label for solid dark lines with $V_g = 4 \times 10^{-6}\,\text{m}^3/\text{mol}$ and $V_Q = 6 \times 10^{-6}\,\text{m}^3/\text{mol}$ indicates solutions using preferred activation volumes as discussed in Section B.

C. Analytical solution for 1-D rheology-dependent mantle flow in N layers

To implement composite rheology in the upper mantle, we must combine both Newtonian Poiseuille flow (*PFn1*) and plug flow (*PFn3*) models. For an assigned Newtonian rheology for the mantle transition zone, we only use the *PFn1* model. We apply Equations 3 and 7.2, and the boundary conditions shown in Figure S3 and summarized below:

$$v_{x,1}(z_0) = U_p \tag{S3}$$

$$v_{x,N}(z_N) = 0 \tag{S4}$$

at z_i: $\tau_i(bottom\ boundary\ of\ ith\ layer) = \tau_{i+1}(top\ boundary\ of\ ith + 1\ layer)$ $\qquad$ (S5)

at z_i: $v_{x,i}(bottom\ boundary\ of\ ith\ layer) = v_{x,i+1}(top\ boundary\ of\ ith + 1\ layer)$ $\qquad$ (S6)

This yields a set of equations:

$$\frac{\partial p}{\partial x} z_i + C_i = \frac{\partial p}{\partial x} z_i + C_{i+1} \rightarrow C_i = C_{i+1} \tag{S7}$$

$$A_{PFn1,i}\left[\frac{1}{2}\frac{\partial p}{\partial x}z_i^2 + C_i z_i\right] + A_{PFn3,i}\left[\begin{array}{c}\frac{1}{4}\left(\frac{\partial p}{\partial x}\right)^3 z_i^4 + C_i\left(\frac{\partial p}{\partial x}\right)^2 z_i^3 \\ +\frac{3}{2}C_i^2 \frac{\partial p}{\partial x}z_i^2 + C_i^3 z_i\end{array}\right] + k_i =$$

$$A_{PFn1,i+1}\left[\frac{1}{2}\frac{\partial p}{\partial x}z_i^2 + C_{i+1} z_i\right] + A_{PFn3,i+1}\left[\begin{array}{c}\frac{1}{4}\left(\frac{\partial p}{\partial x}\right)^3 z_i^4 + C_{i+1}\left(\frac{\partial p}{\partial x}\right)^2 z_i^3 \\ +\frac{3}{2}C_{i+1}^2 \frac{\partial p}{\partial x}z_i^2 + C_{i+1}^3 z_i\end{array}\right] + k_{i+1} \tag{S8}$$

We linearize the equations by grouping the terms in Equations S7 and S8 such that the terms with first degree C's and k's (constants of integration) are on the left side of the equation and the remaining terms are on the right side. Then, we can express the

Figure S3. Boundary conditions for our 1D model with N layers in terms of stress τ_i and horizontal velocity $v_{x,i}$ where i is the layer number. The C_i and k_i integration constants in Equation 3 for stress and Equation 7.2 for flow velocity are determined, which allows us to solve stresses and flow velocities within the model.

boundary conditions for the layered system as $M\mathbf{R}=\mathbf{A}$ where vector $\mathbf{R}$ contains the constants of integration (C's and k's) and vector $\mathbf{A}$ has the higher degree C's:

$$
\begin{pmatrix}
a_{PFn1,1}+a_{PFn3,1} & 1 & 0 & 0 & 0 & 0 & \cdots & 0 & 0 & 0 & 0 \\
a_{PFn1,1}+a_{PFn3,1} & 1 & -(a_{PFn1,2}+a_{PFn3,2}) & -1 & 0 & 0 & \cdots & 0 & 0 & 0 & 0 \\
1 & 0 & -1 & 0 & 0 & 0 & \cdots & 0 & 0 & 0 & 0 \\
0 & 0 & a_{PFn1,2}+a_{PFn3,2} & 1 & -(a_{PFn1,3}+a_{PFn3,3}) & -1 & \cdots & 0 & 0 & 0 & 0 \\
0 & 0 & 1 & 0 & -1 & 0 & \cdots & 0 & 0 & 0 & 0 \\
\vdots & \vdots & \vdots & \vdots & \vdots & \vdots & \ddots & \vdots & \cdots & \vdots & \vdots \\
0 & 0 & 0 & 0 & 0 & 0 & \cdots & a_{PFn1,N-1}+a_{PFn3,N-1} & 1 & -(a_{PFn1,N}+a_{PFn3,N}) & -1 \\
0 & 0 & 0 & 0 & 0 & 0 & \cdots & 1 & 0 & -1 & 0 \\
0 & 0 & 0 & 0 & 0 & 0 & \cdots & 0 & 0 & a_{PFn1,N}+a_{PFn3,N} & 1
\end{pmatrix}
\begin{pmatrix}
C_1 \\ k_1 \\ C_2 \\ k_2 \\ C_3 \\ k_3 \\ \vdots \\ C_{N-1} \\ k_{N-1} \\ C_N \\ k_N
\end{pmatrix}
$$

$$
=
\begin{pmatrix}
-(b_{PFn1,1}+b_{PFn3,1})+U_p \\
-(b_{PFn1,1}+b_{PFn3,1})+(b_{PFn1,2}+b_{PFn3,2}) \\
0 \\
-(b_{Pn1F,2}+b_{PFn3,2})+(b_{PFn1,3}+b_{PFn3,3}) \\
0 \\
\vdots \\
-(b_{PFn1,N-1}+b_{PFn3,N-1})+(b_{PFn1,N}+b_{PFn3,N}) \\
0 \\
-(b_{PFn1,N}+b_{PFn3,N})
\end{pmatrix}
\tag{S9}
$$

where

$$a_{PFn1,i} = A_{PFn1,i}\, z_i \tag{S10}$$

$$a_{PFn3,i} = A_{PFn3,i}\left(\frac{\partial p}{\partial x}\right)^2 z_i^{\,3} \tag{S11}$$

$$b_{PFn1,i} = \frac{1}{2}A_{PFn1,i}\frac{\partial p}{\partial x} z_i^{\,2} \tag{S12}$$

$$b_{PFn3,i} = A_{PFn3,i}\left[\begin{array}{l} \frac{1}{4}\left(\frac{\partial p}{\partial x}\right)^3 z_i^{\,4} + \\[4pt] +\frac{3}{2}C_i^{\,2}\frac{\partial p}{\partial x} z_i^{\,2} + C_i^{\,3} z_i \end{array}\right] \tag{S13}$$

The terms $A_{PFn1,i}$ and $A_{PFn3,i}$ for the upper mantle are defined in Equations 5.3 and 5.4, respectively. For the mantle transition zone (MTZ), $A_{PFn1,i} = 2/\eta_{MTZ}$ and $A_{PFn3,i} = 0$. The higher degree C_i terms in Equation S13 or in vector $\mathbf{A}$ are considered constant and we initially guess them to be the same for every layer i (as in Equation S7) to determine the C_i and k_i in vector $\mathbf{R}$ by inversion ($\mathbf{R}=M^{-1}\mathbf{A}$). Then, in every iteration, we update C_i in vector $\mathbf{A}$ with the calculated C_i in vector $\mathbf{R}$ until their absolute difference is $\leq 10^{-6}$. Then, stresses (Equation 3) and velocities (Equation 7.2) with depth can be calculated using the derived C_i and k_i from vector $\mathbf{R}$.

D. Iteration scheme to compute steady state grain size and stress evolution

The $A_{PFn1,i}$ and $A_{PFn3,i}$ parameters used to calculate stress τ and horizontal velocity v_x (Section C) depend on grain-size, which evolves with time (Equation S16). Both τ and v_x reach a steady state, which is determined by employing the scheme below:

t_0:   *assume constant d_0 $\rightarrow$ calculate v_{x,t_0} and τ_{t_0}*

$t_1 = t_0 + \Delta t$:   *calculate Δd_1 and d_1 $\rightarrow$ calculate v_{x,t_1} and τ_{t_1}*

$t_2 = t_1 + \Delta t$:   *calculate Δd_2 and d_2 $\rightarrow$ calculate v_{x,t_2} and τ_{t_2}*

$$\vdots$$

$$\boldsymbol{t_k = t_{k-1} + \Delta t}: \quad calculate\ \Delta d_k\ and\ d_k\ \rightarrow calculate\ v_{x,t_k}\ and\ \tau_{t_k}$$

where

$$t_k = k\Delta t = \text{grain size evolution time}$$

$$\Delta t = \text{change in time or time interval}$$

$$d_k = \text{new grain size structure after } t_k \text{ (Equation S14)}$$

$$\Delta d_k = \text{change in grain size after } t_k \text{ (Equation S15)}$$

$$v_{x,t_k} = \text{horizontal velocity profile of the flow at } t_k$$

$$\tau_{t_k} = \text{stress profile induced by the flow at } t_k$$

After time t_k (which is $t_{k-1} + \Delta t$), we determine the new grain size structure d_k:

$$d_k = d_{k-1} + \Delta d_k \tag{S14}$$

where Δd_k is estimated by multiplying the grain-size change rate $\dot{d}_{k-1}$ at t_{k-1} by Δt:

$$\Delta d_k = \Delta t[\dot{d}_{k-1}] = \Delta t[\dot{d}_{gg,k-1} - \dot{d}_{dr,k-1}] \tag{S15}$$

Here $\dot{d}_{k-1}$ is estimated using the grain size evolution model of Austin and Evans (2007) (AE07),

$$AE07\ model: \dot{d} = p_g^{-1} d^{1-p_g} G_o \exp\left(-\frac{E_g + PV_g}{RT}\right) - \chi c^{-1} \gamma^{-1} \sigma \dot{\varepsilon}_{disl} d^2 \tag{S16}$$

where the first term describes the grain growth rate $\dot{d}_{gg}$, and the second term describes dynamic recrystallization rate $\dot{d}_{dr}$ that results in grain size reduction. So, the $\dot{d}_{gg,k-1}$ and $\dot{d}_{dr,k-1}$ terms in Equation S15 correspond to the first and second terms in Equation S16. The constants used in the calculation of $\dot{d}$ (as described by Equations S16 and S15) are summarized in Table S1. Using the new d_k, we recalculate the horizontal velocity, shear stress, and viscosity structures. We iterate this process until a steady state grain size is reached at steady-state time t_{ss} (typically << 1 Myr, criterion is discussed in Section E).

Table S1. Grain size evolution parameters are taken from Behn et al. (2009) since they are calibrated to laboratory data, and the flow law parameters are from Hirth and Kohlstedt (2003).

Symbol	Description	Value	Units
$\dot{d}_{gg}$	Grain growth rate		m/s
$\dot{d}_{dr}$	Dynamic recrystallization rate		m/s
τ	Shear stress		Pa
σ	Differential stress (2τ)		Pa
p_g	Grain growth exponent	3	

G_o(dry)	Grain growth constant for 50 ppm H/Si	1.5×10^{-5}	$m^{p_g} s^{-1}$
G_o(wet)	Grain growth constant for 1000 ppm H/Si	4.5×10^{-4}	$m^{p_g} s^{-1}$
E_g	Activation energy for grain growth	350	kJ/mol
V_g	Activation volume for grain growth	4×10^{-6}	m^3/mol
λ	Reciprocal of strain required for new grain size	10	
χ	Fraction of work done by dislocation to ground boundary area	0.1	
c	Geometrical constant	3	
γ	Average specific grain boundary energy	1	J/m^2

		For olivine		s^{-1}
$\dot{\varepsilon}_{disl}$	Dislocation creep strain rate	DRY	WET	
A_{disl}	Dislocation creep prefactor	1.1×10^5	30	$MPa^{-3.5} s^{-1}$
n_{disl}	Dislocation creep stress exponent	3.5	3.5	
p_{disl}	Dislocation creep grain size exponent	0	0	
r_{disl}	Dislocation creep water exponent	0	1.2	
α_{disl}	Constant for melt factor	45	45	
E_{disl}	Dislocation creep activation energy	530	480	kJ/mol
V_{disl}	Dislocation creep activation volume	15×10^{-6}	11×10^{-6}	m^3/mol

		For olivine		s^{-1}
$\dot{\varepsilon}_{diff}$	Diffusion creep strain rate	DRY	WET	
A_{diff}	Diffusion creep prefactor	1.5×10^9	1×10^6	$MPa^{-3.5} s^{-1}$
n_{diff}	Diffusion creep stress exponent	1	1	
p_{diff}	Diffusion creep grain size exponent	3	3	
r_{diff}	Diffusion creep water exponent	0	1	
α_{diff}	Constant for melt factor	30	30	
E_{diff}	Diffusion creep activation energy	375	335	kJ/mol
V_{diff}	Diffusion creep activation volume	6×10^{-6}	4×10^{-6}	m^3/mol

E. Convergence criterion for grain size evolution

To determine the steady-state time t_{ss}, we employ a convergence criterion of:

$$\frac{\Delta d_{norm}}{d_{norm}} \leq \vartheta \qquad \text{(S17)}$$

where ϑ is the limit for convergence, Δd_{norm} is the depth-averaged norm of grain size change, and d_{norm} is the depth-averaged norm of grain size. As a convergence criterion, we use Equation S18.1 for a chosen timestep Δt. At time t_k, the parameters in Equation S17 are calculated as:

$$\vartheta = 5 \times 10^{-4} \left(\frac{\Delta t}{1000 \ yr} \right) \tag{S18.1}$$

$$\Delta d_{norm} = \frac{\sqrt{\sum_{i=1}^{N+1}(d_k - d_{k-1})^2 \Delta z}}{\sum_{i=1}^{N+1} \Delta z} \tag{S18.2}$$

$$d_{norm} = \frac{\sqrt{\sum_{i=1}^{N+1} d_k^2 \Delta z}}{\sum_{i=1}^{N+1} \Delta z} \tag{S18.3}$$

When the criterion in Equation S17 is met, $t_k \sim t_{ss}$.

F. Additional analyses at steady-state

F.1 Effect of initial grain-size

We compare two steady-state calculations that are the same except for different initial olivine grain-sizes (1 mm or 10 mm), which produces flow via CF above a 10^{21} Pa·s mantle transition zone as shown in Figure S4a. Such a flow configuration dominates
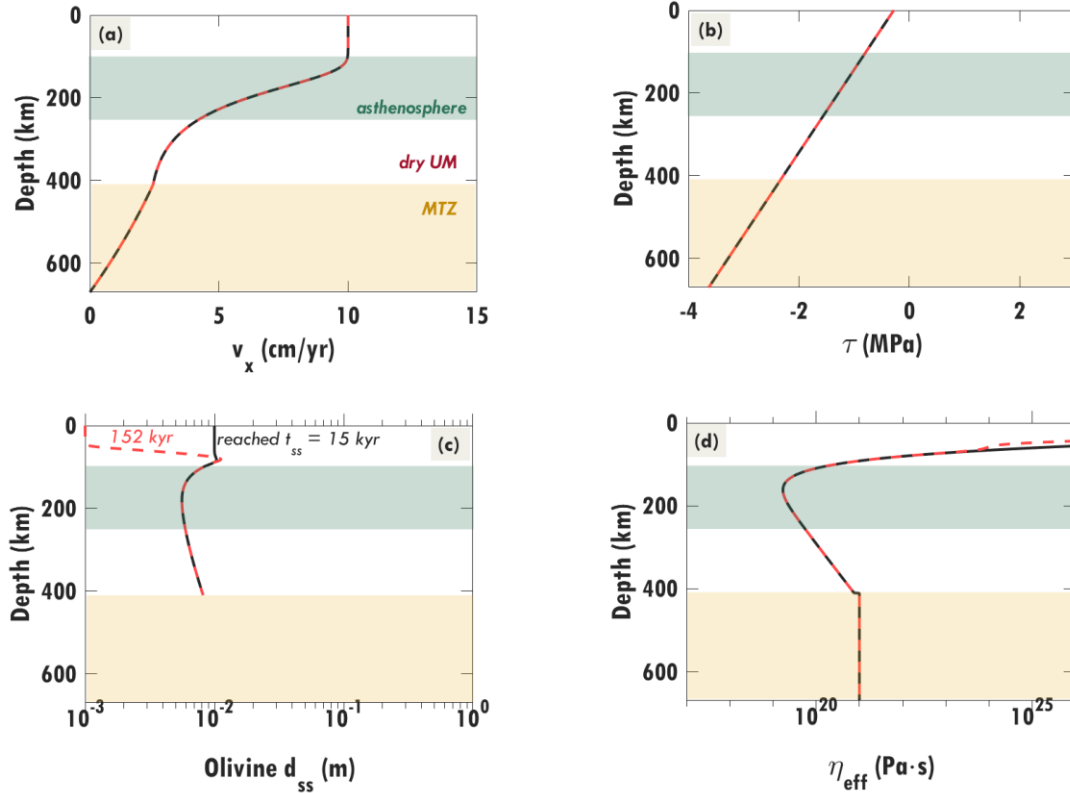

Figure S4. Effect of initial grain size (1 mm and 10 mm for the red dashed and black lines, respectively) on the steady-state (a) upper mantle flow, (b) induced shear stresses, (c) grain-size structure, and (d) effective viscosity. We assume dry conditions, and that the 60 Myr old oceanic upper mantle and mantle transition zone are deformed by plate motion of 10 cm/yr and a pressure gradient of -5kPa/km. Until the flow reaches steady state, grain size changes according to the grain size evolution model AE07 (Austin and Evans, 2007). Flow additionally alters the grain-size structure, which in turn changes the flow and rheology with time. The flow eventually reaches steady state after a time t_{ss}=152 kyr for an initial grain size of 1 mm and t_{ss}=15 kyr for an initial grain size of 10 mm (see Supplementary Information D). The timesteps Δt used for 1-mm and 10-mm flow models are 10 yr and 100 yr, respectively.

because of large viscosities in the upper mantle and mantle transition zone (Figure S4d). Initially smaller (1 mm) and larger (10 mm) grain-sizes evolve to the same steady-state grain-size structure (except for the stiff undeforming lithosphere, Figure S4c) and the same steady-state upper mantle flow (Figure S4a) with the same stress profile (Figure S4b). Clearly, the choice of initial grain-size does not affect the system's eventual steady-state but it does affect the time it takes the grain size to reach steady state. A larger initial grain size (i.e., 10 mm) stabilizes faster (15 kyr) compared to a smaller grain size (1 mm, 152 kyr), because large grain-sizes subdivide rapidly (Equation S16).

F.2 Effect of grain-size evolution model

Hall and Parmentier (2003) provide another grain-size evolution model (HP03 model):

$$HP03\ model: \quad \dot{d} = p_g^{-1} d^{1-p_g} G_o \exp\left(-\frac{E_g + PV_g}{RT}\right) - \lambda \dot{\varepsilon}_{disl} d \tag{S19}$$

The grain-size structure stabilizes faster when using the AE07 model ($t_{ss} = 478\ kyr$) compared to using the HP03 model (598 kyr) because of AE07's strong dependence on grain-size (Figure S5c). Although the HP03 model (red dashed line, Figure S5c)
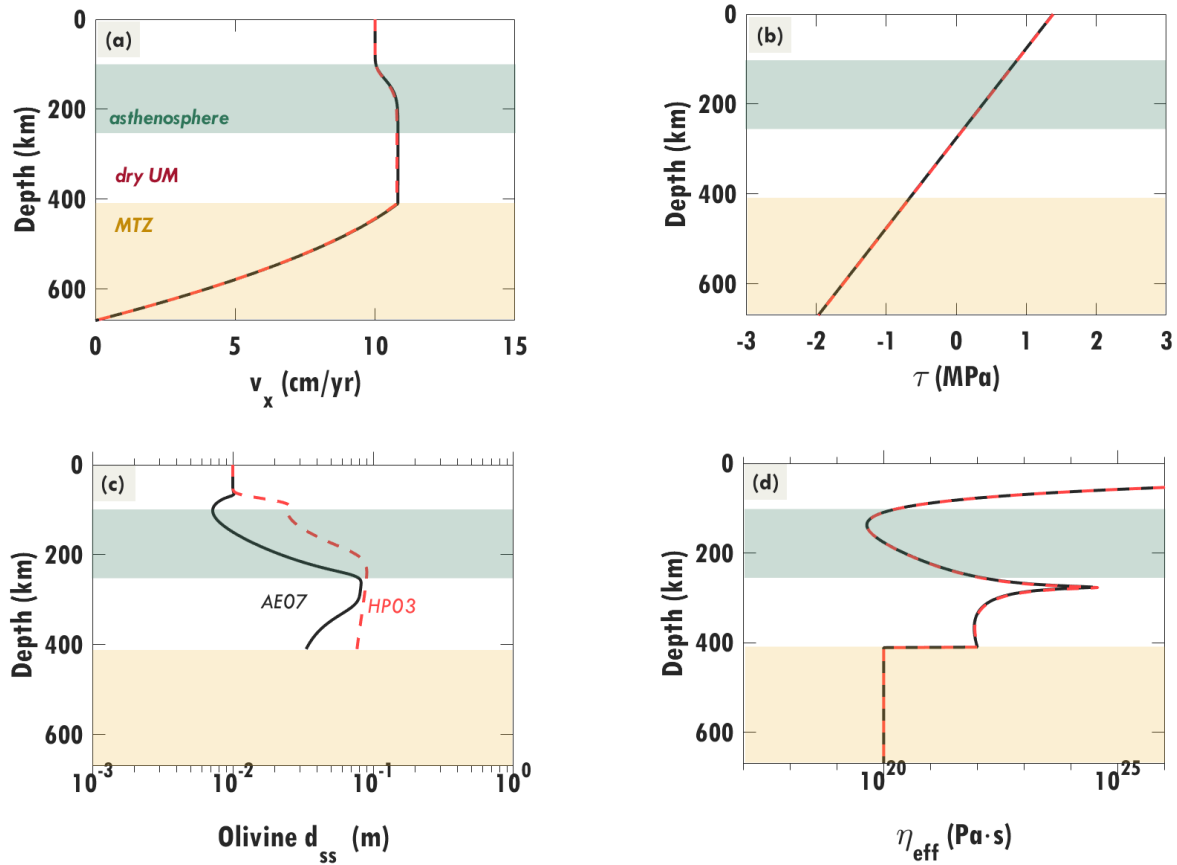

Figure S5. Effect of grain size evolution model (HP03 (Hall and Parmentier, 2003) for the red dashed line and AE07 (Austin and Evans, 2007) for the black line) on the steady-state (a) upper mantle flow, (b) induced shear stresses, (c) grain-size structure (initially 10 mm grain size), and (d) viscosity. The flow conditions considered are the same as in Figure S4, except that the mantle transition zone (MTZ) is assumed to have 10^{20} Pa·s viscosity. The timesteps Δt used for the HP03 and AE07 grain-size evolution models are 1000 yr and 100 yr, respectively.

predicts larger grain sizes than does the AE07 model (black line), their flow configurations (*PF*, Figure S5a), stress profiles (Figure S5b), and viscosities (Figure S5d) are nearly the same.

F.3 Effect of contrasting rheologies between the upper mantle and MTZ

In Section 4, the comparable effective viscosities of upper mantle and mantle transition zone result in a *CF*-dominated dry upper mantle and a *PF*-dominated wet upper mantle. However, with contrasting rheologies, the dry upper mantle can accommodate a *PF* configuration (case ii, Figure S6a) and a *CF* configuration in wet upper mantle
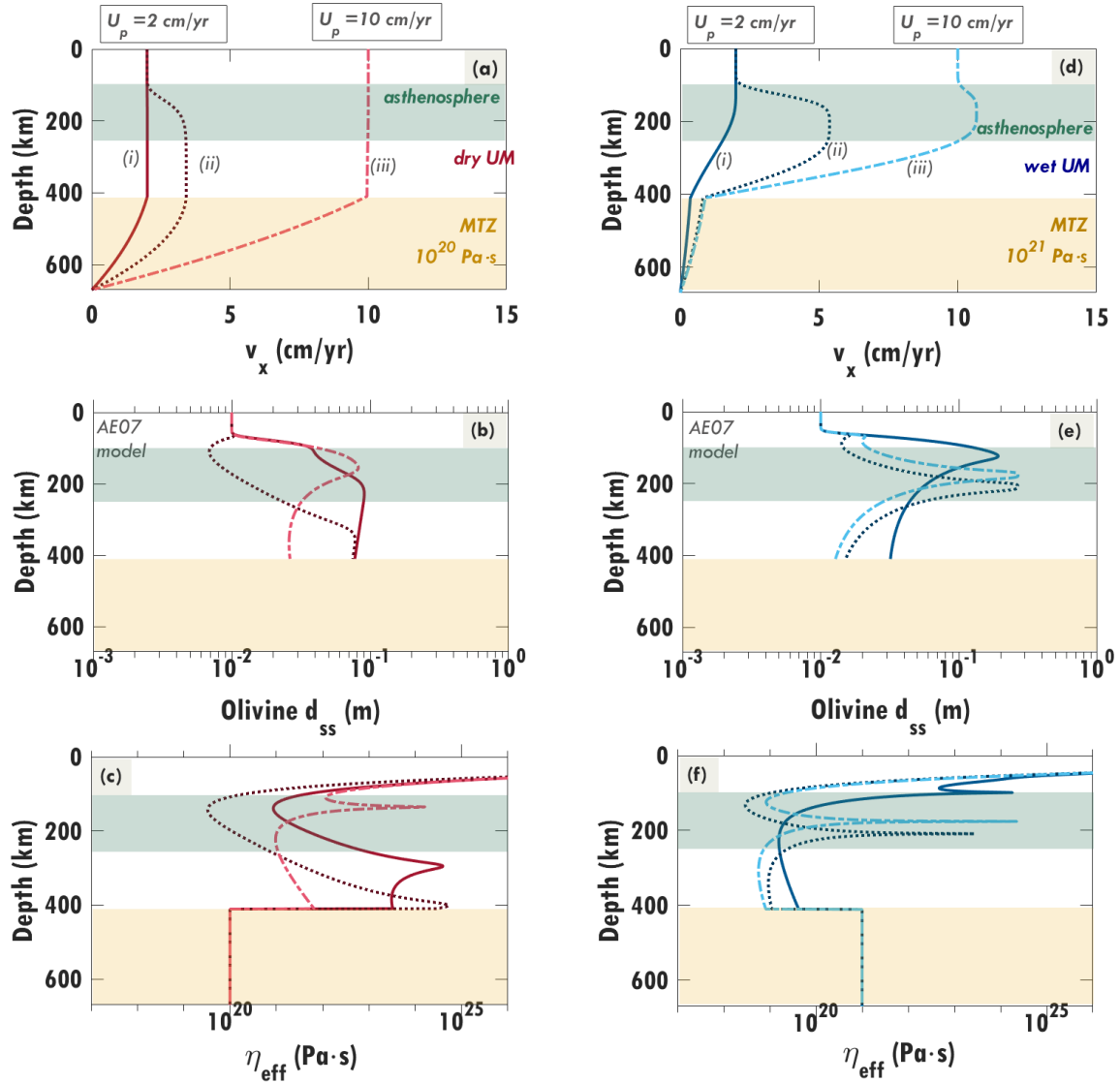

Figure S6. Effect of contrasting rheologies between upper mantle (UM) and MTZ on the steady state (a, d) flow, (b, e) grain size structure, and (c, f) viscosity for (a-c) dry and (d-f) wet conditions. Different combinations of plate velocity and horizontal pressure gradient (labeled as i, ii and iii) are considered, and are the same as in Figure 4. For dry upper mantle, the assigned mantle transition zone (MTZ) viscosity is 10^{20} Pa·s, and for wet upper mantle it is 10^{21} Pa·s. The less viscous MTZ viscosity allows for a *PF* (Poiseuille flow) configuration to dominate in the more viscous upper mantle. Otherwise, *CF* (Couette flow) may dominate unless the pressure gradient is large enough to drive *PF* that exceeds plate velocity. The initial grain-size for each calculation is 10 mm. A timestep Δt of 1000 yr is used for case (i), and 100 yr for cases (ii) and (iii).

(case i, Figure S6d). The less viscous mantle transition zone below dry upper mantle (Figure S6c) allows a pressure-driven flow within the upper mantle (case ii, Figure S6a). In contrast, the more viscous mantle transition zone below the wet upper mantle (Figure S6f) can shut down pressure-driven flow unless the pressure gradient is large enough (cases ii and iii, Figure S6d) to drive PF that exceeds the plate-driven flow.

F.4 Effect of small melt fraction on upper mantle flow and rheology

We consider a -1 kPa/km pressure gradient in the wet mantle and a 2-cm/yr plate velocity, which result in the $PFn3$ flow configuration under dislocation creep for the viscosity and grain size structures shown in Figure S7 (blue lines). Adding a small amount of melt (< 0.1%, Figure S7a) reduces the viscosity by a factor of ~0.98, which yields negligible changes to the flow pattern, rheology and grain sizes (orange line, Figure S7).
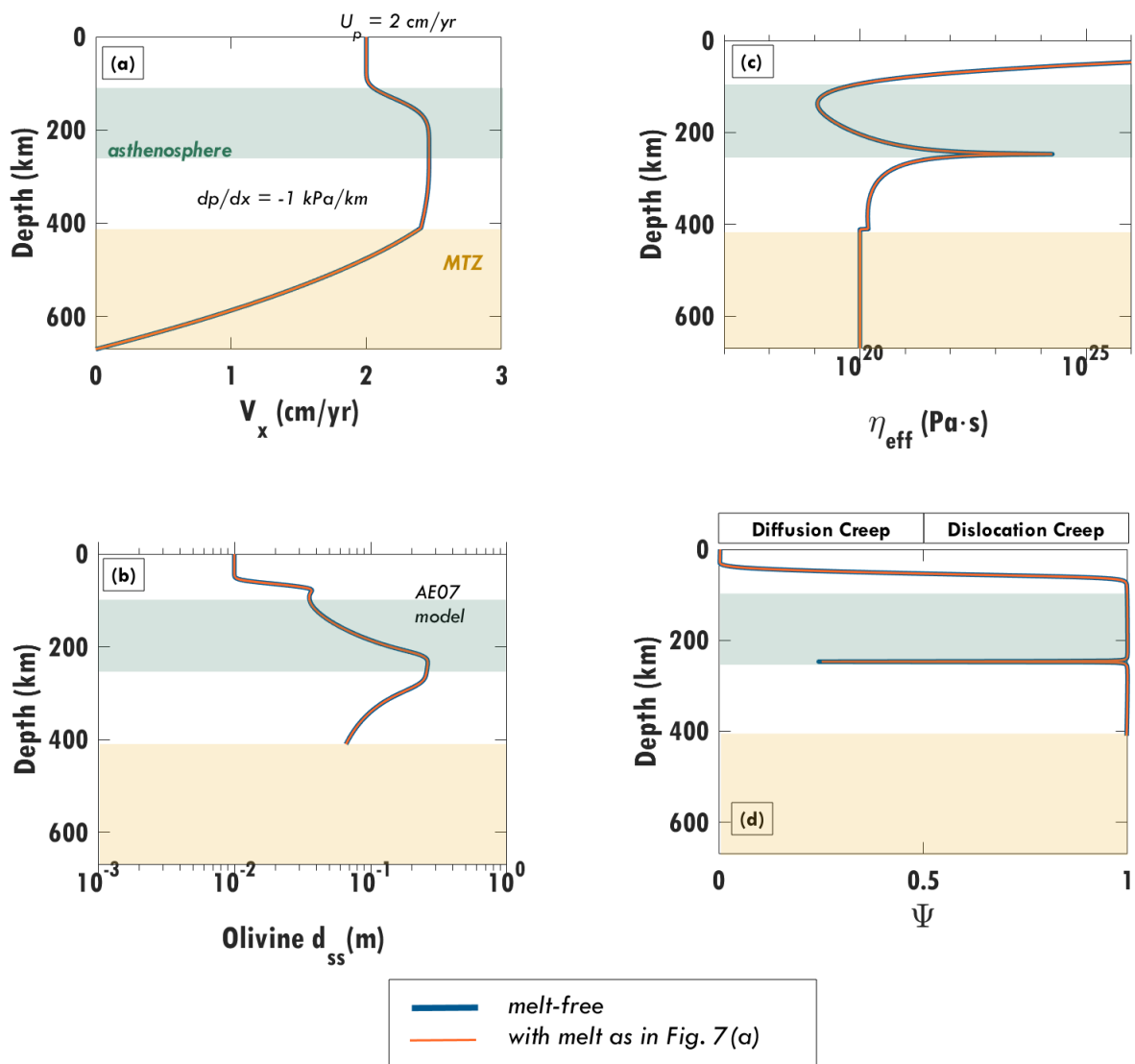

Figure S7. Effect of excluding melt (blue line) vs. including melt (orange line) on steady-state upper mantle (a) flow, (b) olivine grain sizes, (c) viscosity, and (d) dominant deformation mechanism. This calculation use a 60 Myr old oceanic upper mantle with 2 cm/yr plate velocity, a -1 kPa/km pressure gradient, and grain-size evolution model AE07 (Austin and Evans, 2007) with a timestep Δt of 1000 yr.

F.5 Different flow configurations in dry and wet upper mantle

The flow configurations and rheological structures for the different plate velocity and pressure gradient combinations and MTZ viscosities are shown in Figures S8 and S9 for dry and wet conditions, respectively, as discussed in Section 7.
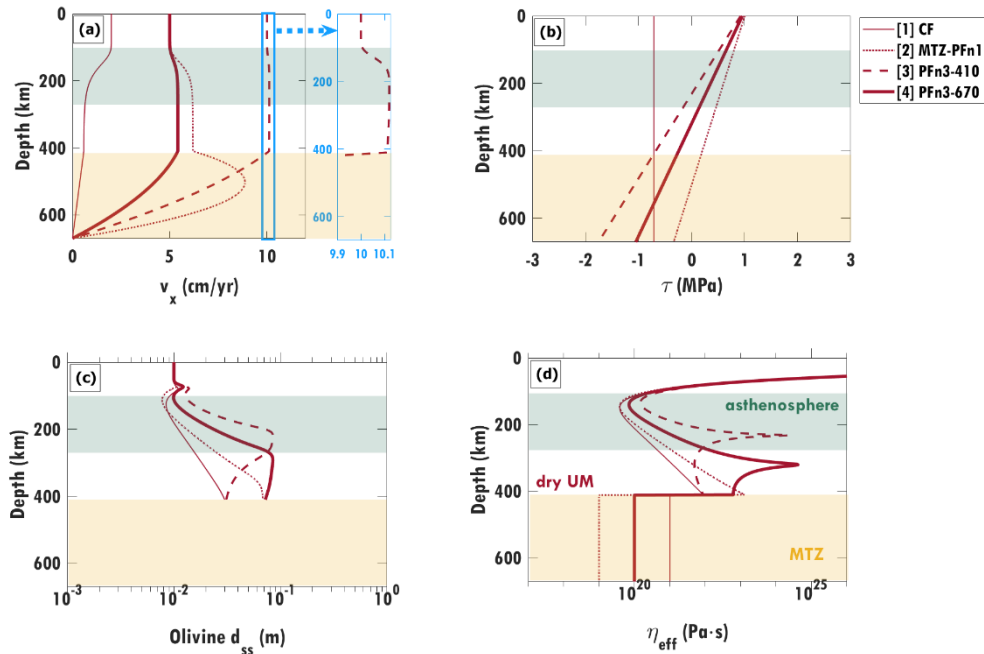

Figure S8. The (a) four flow configurations for dry (50 ppm H/Si) upper mantle and their associated (b) stresses, (c) grain-sizes, and (d) viscosity structures. The corresponding plate speed and pressure gradient combinations used to produce such flows are shown in Figure 8b.1 (in red rectangles).
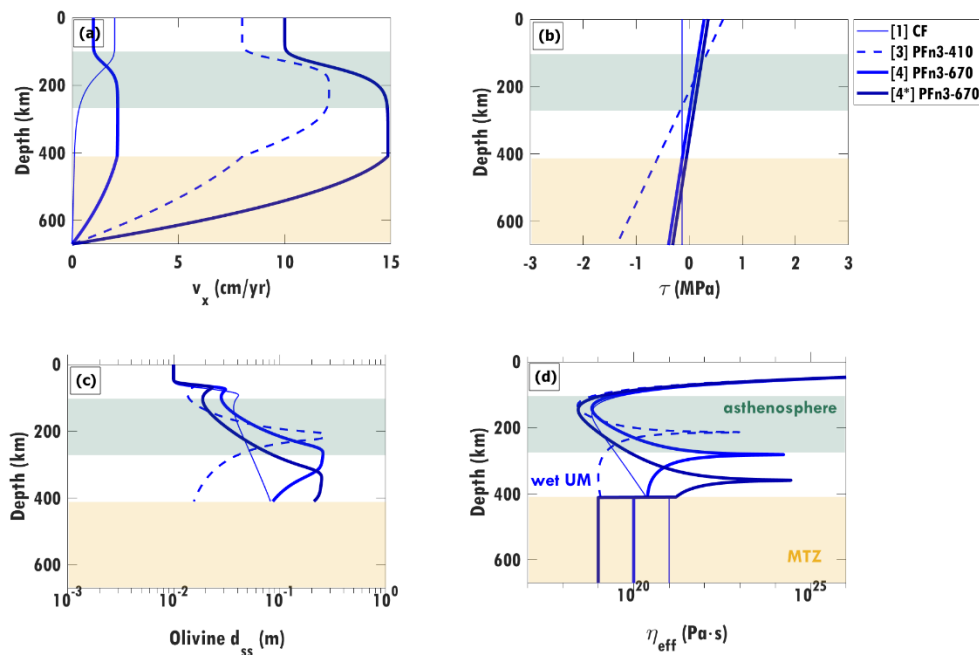

Figure S9. The (a) four flow configurations plausible for wet (1000 ppm H/Si) upper mantle and their associated (b) stresses, (c) grain-sizes, and (d) viscosity structures. The corresponding plate speed and pressure gradient combinations used to produce such flows are shown in Figure 8b.2 (in blue rectangles).

References

Austin, N.J., and Evans, B. (2007). Paleowattmeters: A scaling relation for dynamically recrystallized grain size. *Geology, 35*, 343-346. doi:10.1130/G23244A.1

Behn, M., Hirth, G. and Elsenbeck II, J. R. (2009). Implications of grain size evolution on the seismic structure of the oceanic upper mantle. *Earth and Planetary Science Letters, 282*, 178-189. doi: 10.1016/j.epsl.2009.03.014

Dalton, C., Ekström, G., and Dziewonski, A. (2008). The global attenuation structure of the upper mantle. J. *Geophys. Res. 113*, B09303. doi:10.1029/2007JB005429

Faul, U. and Jackson, I. (2005). The seismological signature of temperature and grain size variations in the upper mantle. *Earth and Planetary Science Letters, 234*, 119-134. doi:10.1016/j.epsl.2005.02.008

Hall, C. and Parmentier, E.M. (2003). Influence of grain size evolution on convective instability. *Geochem. Geophys. Geosyst., 4*, 1029. doi:10.1029/2002GC000308

Hirth, G., and Kohlstedt, D. (2003). Rheology of the Upper Mantle and the Mantle Wedge: A View from the Experimentalists. *Inside the Subduction Factory, Geophysical Monograph, 138*, 83-105.

Jackson, I., and Faul, U. (2010). Grainsize-sensitive viscoelastic relaxation in olivine: Towards a robust laboratory-based model for seismological application. *Physics of the Earth and Planetary Interiors, 183*, 151-163. doi:10.1016/j.pepi.2010.09.005

Karaoglu, H. and Romanowicz, B. (2018). Inferring global upper-mantle shear attenuation structure by waveform tomography using spectral element method. *Geophys. J. Int., 213*, 1536-1558. doi: 10.1093/gji/ggy030

Karato, S.-i. (1993). Importance of anelasticity in the interpretation of seismic tomography. *Geophys. Res. Lett., 20*, 1623-1626. doi:10.1029/93GL01767

Nettles, M. and Dziewonski, A. (2008). Radially anisotropic shear velocity structure of the upper mantle globally and beneath North America. *Journal of Geophysical Research, 113*, B02303. doi:10.1029/2006JB004819

Romanowicz, B. (1995). A global tomographic model of shear attenuation in the upper mantle. *Journal of Geophysical Research, 100(B7)*, 12375–12394. doi:10.1029/95jb00957

Sammis, C.G., Smith, J.C., Shubert, G. (1981). A critical assessment of estimation methods for activation volume. J. Geophys. Res., 86, 10707-10718. doi: 10.1029/JB086iB11p10707

Stixrude, L., and Lithgow-Bertelloni, C. (2005). Mineralogy and elasticity of the oceanic upper mantle: Origin of the low-velocity zone. *J. Geophys. Res., 110*, B03204, doi:10.1029/2004JB002965.